Atomically Flat, 2D Edge-Directed Self-Assembly of Block Copolymers

Jang Hwan Kim, Hyeon U Jeong, Hye-In Yeom, Kyu Hyo Han, Geon Gug Yang, Hee jae Choi, Jong Min Kim, Sang-Hee Ko Park, Hyeong Min Jin,* Jaeup U. Kim,* and Sang Ouk Kim*

Nanoscale shape engineering is an essential requirement for the practical use of 2D materials, aiming at precisely customizing optimal structures and properties. In this work, sub-10-nm-scale block copolymer (BCP) self-assembled nanopatterns finely aligned along the atomic edge of 2D flakes, including graphene, MoS$_2$, and h-BN, are exploited for reliable nanopatterning of 2D materials. The underlying mechanism for the alignment of the self-assembled nanodomains is elucidated based on the wetting layer alternation of the BCP film in the presence of intermediate 2D flakes. The resultant highly aligned nanocylinder templates with remarkably low levels of line edge roughness (LER) and line-width roughness (LWR) yield a sub-10-nm-wide graphene nanoribbon (GNR) array with noticeable switching characteristics (on-to-off ratio up to $\approx 6 \times 10^4$).

1. Introduction

2D materials offer intriguing material properties that are particularly differentiated from those of their bulk counterparts, as driven by the atomic-scale 2D confinement effect.[1–2] In this

regard, 2D materials, such as graphene, molybdenum disulfide (MoS$_2$), and hexagonal boron nitride (h-BN), have exhibited competitive performance in a wide range of applications, including electronics,[3] sensors,[4] catalysts,[5] energy storage, and conversion.[6] Nonetheless, for practical use in real-world applications, it is necessary to precisely optimize and customize the physical and chemical properties of 2D materials. Nanoscale shape engineering of a 2D basal plane is a reliable and viable route for this purpose.

A variety of nanoscale shape-engineering methodologies have been introduced for 2D materials, including atomic force microscopy lithography,[7] electron-beam lithography,[8] and scanning tunneling microscopy based lithography.[9] Block copolymer (BCP) nanolithography is a promising strategy that takes advantage of the inherently scalable parallel formation process for highly periodic ultrafine pattern dimensions down to the sub-5-nm level.[10–11] However, spontaneously organized BCP nanopatterns generally suffer from random orientation of nanodomains with many structural defects. Thus, numerous efforts have been devoted to direct BCP self-assembly for the orientational and positional ordering of nanodomains, particularly by means of synergistic integration with conventional lithography.[12–16] Unfortunately, the unavoidable pattern roughness of the guide pattern prepared using typical photolithography commonly results in a deteriorated quality of BCP self-assembled nanopatterns with relatively high levels of defectivity, line-edge roughness (LER), and line-width roughness (LWR).

In this study, BCP nanopatterns were directed by the edges of 2D materials with atomic-level minimal roughness. The presence of intermediate 2D flakes, such as graphene, MoS$_2$, and h-BN, dramatically influences the interfacial wetting characteristics of self-assembled BCP thin films on typical device substrates. Notably, despite its well-known wetting transparency,[17] atomically thin monolayer graphene successfully induces favorable wetting of PS domains mediated by the specific π–π stacking interaction with phenyl side groups in PS.[18] Such a wetting contrast generally results in sharp step confinement for self-assembled BCP nanodomains along the flake edges, exhibiting an unprecedented high degree of ordering of BCP nanopatterns with low degrees of LER/LWR. Owing to the high uniformity and periodicity of self-assembled BCP nanodomains, a sub-10-nm-scale graphene nanoribbon (GNR) array templating

J. H. Kim, K. H. Han, G. G. Yang, H. j. Choi, S. O. Kim
National Creative Research Initiative (CRI) Center for Multi-Dimensional
Directed Nanoscale Assembly
Department of Materials Science and Engineering
KAIST
Daejeon 34141, Republic of Korea
E-mail: sangouk.kim@kaist.ac.kr

J. H. Kim, K. H. Han, G. G. Yang, H. j. Choi, S. O. Kim
KAIST Institute for NanoCentury
Korea Advanced Institute of Science and Technology (KAIST)
Daejeon 34141, Republic of Korea

H. U. Jeong, J. U. Kim
Department of Physics
UNIST
Ulsan 44919, Republic of Korea
E-mail: jukim@unist.ac.kr

H.-I. Yeom, J. M. Kim, S.-H. K. Park
Department of Materials Science and Engineering
KAIST
Daejeon 34141, Republic of Korea

H. M. Jin
Department of Organic Materials Engineering
Chungnam National University
Daejeon 34134, Republic of Korea
E-mail: hyeongmin@cnu.ac.kr

The ORCID identification number(s) for the author(s) of this article
can be found under https://doi.org/10.1002/adma.202207338.

**ADVANCED
SCIENCE NEWS**

www.advancedsciencenews.com

**ADVANCED
MATERIALS**

www.advmat.de

from the BCP nanopattern demonstrated noticeable switching characteristics (on-to-off ratio of ≈6 × 10^4).

2. Results and Discussion

A schematic of the 2D edge-directing BCP self-assembly is shown in **Figure 1**a. Mono- or few-layered flakes of 2D materials, including graphene, MoS$_2$, and h-BN, were mechanically exfoliated from bulk crystals onto SiO$_2$ substrates. Without any further treatment or surface modification, cylinder-forming PS-b-PDMS BCP (M_n of PS and PDMS blocks = 11 and 5 kg mol^{-1}, respectively) was blended with PS homopolymer (M_n = 6.5 kg mol^{-1}) in a weight ratio of 9:1. Next, thin film was spin-coated onto the substrate and thermally annealed (≈280 °C, 3 min) to trigger self-assembly. As shown in the scanning electron microscopy (SEM) images in Figure 1b, 8-nm wide in-plane nanocylinders are highly aligned along the 1 μm and 120 nm wide linear-shaped graphene flakes. The insets in each figure show the orientation mapping of the nanocylinders, demonstrating unidirectional alignment along the longitudinal direction of the flakes. Such directed self-assembly behavior can be universally adapted to other 2D materials. As shown in Figure 1c,d, the BCP nanopatterns were highly aligned along the sharp edges of h-BN and MoS$_2$ flakes. Moreover, this alignment principle is not limited to PS-b-PDMS systems. Other BCP nanopatterns, such as in-plane cylindrical structures of PS-b-P2VP, one of the prevalent high-χ BCPs for the sub-10 nm patterning, could also be successfully aligned along the flake edge (Figure 1e).

For the quantitative analysis of defects in the edge-directed BCP nanopatterns, the defect density was evaluated according to the flake width (Figure S1, Supporting Information). Although the 2D-flake edge is atomically flat, the main reason for the defect formation in the BCP nanopatterns is the incommensurability between the flake width and BCP nanopatterns. Therefore, the smaller the width of the 2D flake, the higher is the probability that the pattern is incommensurable in the limited width, resulting in a higher defect density.

For a systematic understanding of the alignment mechanism from edge-directed assembly, depth profiling of BCP thin films self-assembled on h-BN/SiO$_2$ and bare SiO$_2$ was carried out using time-of-flight secondary-ion mass spectrometry (ToF-SIMS). Because graphene is generally difficult to distinguish from the organic BCP layer, which is also dominated by carbon atoms, h-BN was selected for this analysis. As shown in **Figure 2**a, a few-layered h-BN flake was readily identified on the SiO$_2$ substrate by CB$^-$ ions. For a straightforward comparison, the depth profiles of the BCP thin films thermally annealed on h-BN/SiO$_2$ (Figure 2b) and bare SiO$_2$ (Figure 2c) were collected. The depth profiles at these two interfaces were clearly contrasted.
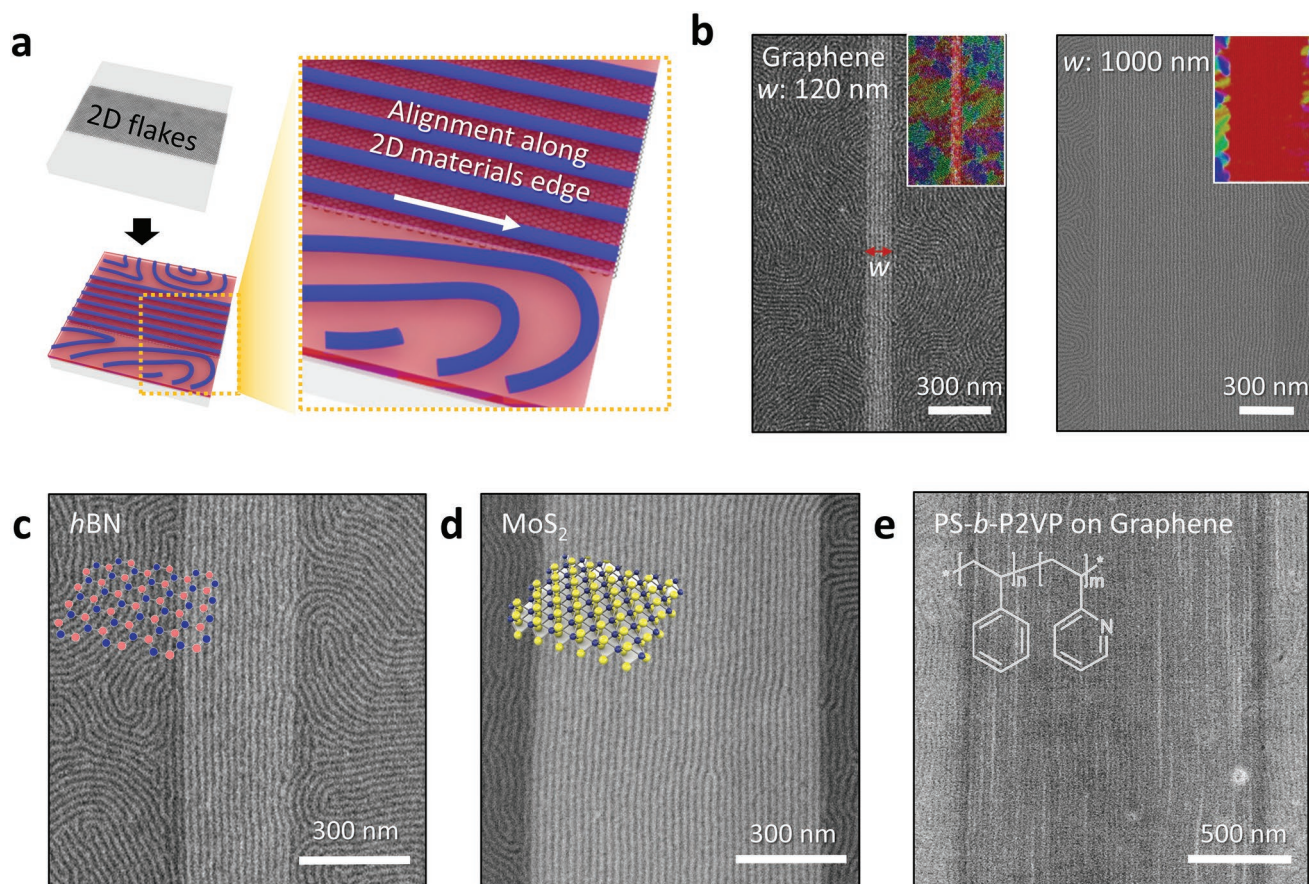

Figure 1. a) Directed self-assembly of block copolymers along 2D flake edge. b–d) Highly aligned self-assembled PS-b-PDMS cylindrical nanostructures on graphene (b), h-BN (c), MoS$_2$ (d). e) Highly aligned PS-b-P2VP cylindrical nanostructure on graphene flake.
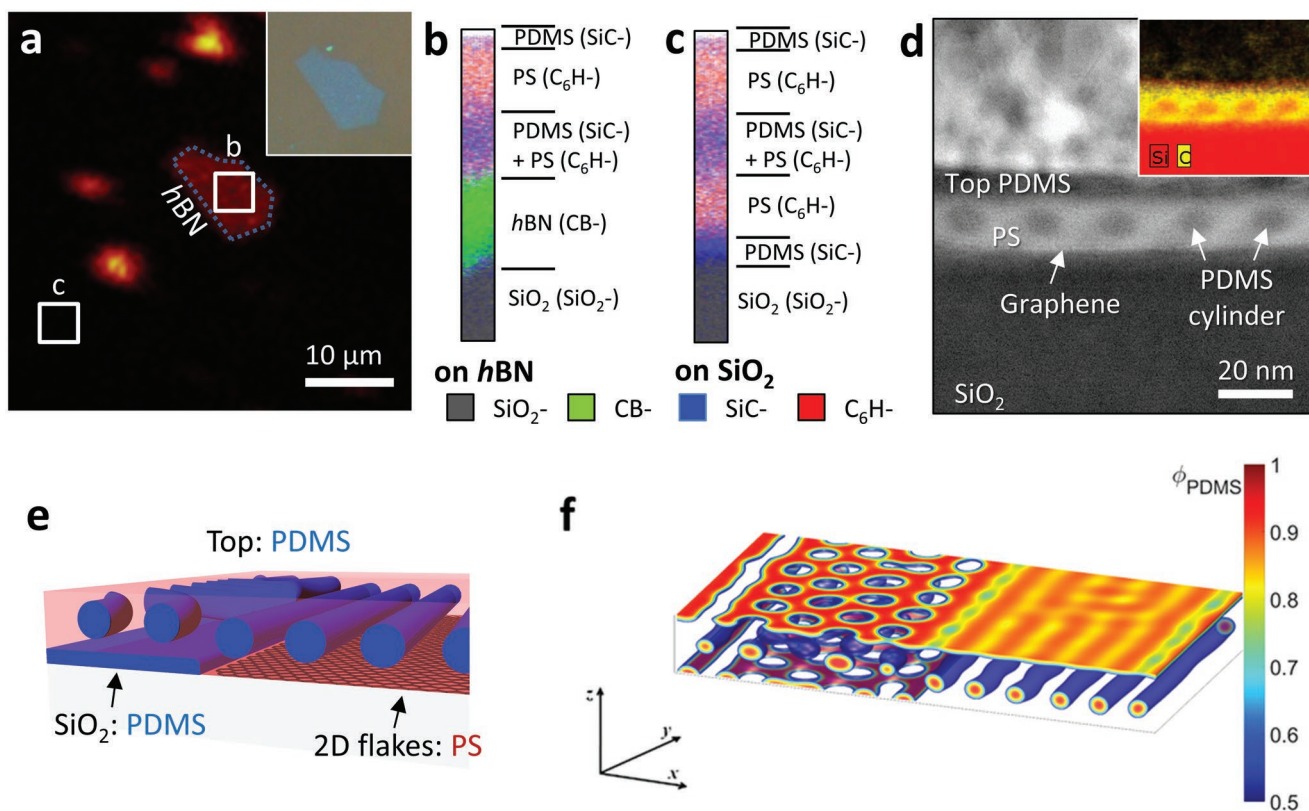
Figure 2. Structural configuration and alignment mechanism of PS-*b*-PDMS cylindrical self-assembly. a) Optical image of *h*-BN flake (inset) and TOF-SIMS image of self-assembled BCP thin film on an *h*-BN flake. b,c) SIMS depth profiles corresponding to the areas b and c in (a). d) TOF-SIMS image (inset) and cross-sectional TEM image of sub-10-nm-wide PS-*b*-PDMS nanopattern self-assembled on a graphene flake. e) Proposed structural configuration of self-assembled nanocylinders at the edge of 2D flakes. f) Cylindrical self-assembly of PS-*b*-PDMS on edge of 2D flake as suggested by SCFT calculation with $\chi N = 18$ and PDMS fraction $f = 0.3$. PS homopolymers (volume fraction 10%) are mixed with the BCPs, and only the minor composition PDMS phase (red and blue colors) is shown.

Figure 2b presents that the self-assembled structure formed on *h*-BN flakes has a very thin PS wetting layer at the bottom interface with *h*-BN, above which in-plane PDMS nanocylinders are self-assembled within the PS matrix. Subsequently, a PS layer appears, and finally, a PDMS layer is formed at the top surface. Because this depth profile is obtained against the sputter etching time rather than the actual thickness, the *h*-BN layer with a significantly lower sputter etching rate than the sparse polymer layer appears exaggerated. In contrast, in the absence of *h*-BN, the PDMS wetting layer lies directly on the SiO₂ substrate, followed by the PS layer (Figure 2c). Subsequently, monolayer in-plane PDMS cylinders are formed within the PS matrix, above which the alternating PS and PDMS layers are stabilized. Cross-sectional TEM confirmed that the PS matrix directly wets the bottom graphene interface, whereas the PDMS layer preferentially wets the top surface, as confirmed by ToF-SIMS (Figure 2d and inset). Figure 2e schematically illustrates the internal structures of the BCP thin films at different surfaces, in accordance with the above-mentioned observations.

Owing to the ultrathin mono- or few-layered 2D flakes (typically <1 nm), it is difficult to provide an effective topographical step to influence the BCP self-assembly behavior. Instead, their surface chemistry could lead to differences in preferential wetting behavior compared to bare SiO₂.[20–20]

Table 1 summarizes the calculated interfacial energies, γ, of different polymer components (PS, PDMS, and P2VP) on various surfaces (2D flakes and SiO₂) (detailed calculations of γ are provided in Supporting information). Because the individual BCP chain has a nanoscale conformation, the non-additivity of nanoparticle interactions can be considered when calculating the interaction with the substrate.[21–22] However, because polymers exist in a molten state (i.e., polymer chains are not isolated but entangled with each other) during phase separation, the interaction between the polymer melt and the substrate can be estimated using a simple harmonic-mean equation. From the calculation, polymers other than PS (e.g., P2VP or PDMS) are expected to wet the bare SiO₂ (γ_{SiO_2-P2VP}, $\gamma_{SiO_2-PDMS} < \gamma_{SiO_2-PS}$), whereas 2D flakes covered with SiO₂ (e.g., graphene, MoS₂, or *h*-BN) are preferred to be wetted by PS ($\gamma_{2D-P2VP}$, $\gamma_{2D-PDMS} > \gamma_{2D-PS}$).

Table 1. Calculated interfacial energies of PS, PDMS, P2VP, and PMMA at various 2D-material surfaces.

γ_{A-B} [mN m⁻¹]	Air	SiO₂[53]	Graphene[54]	MoS₂[54]	*h*-BN[55]
PS[56]	42.6	74.03	**1.69**	**1.54**	**3.80**
PDMS[56]	19.5	**68.84**	3.77	5.64	15.64
P2VP[56]	39.5	**15.01**	38.34	25.68	23.58

**ADVANCED
SCIENCE NEWS**

www.advancedsciencenews.com

**ADVANCED
MATERIALS**

www.advmat.de

Therefore, surface energy modification in the presence of monolayer 2D flakes can lead to a change in wetting behavior.

In general, a single layer of MoS$_2$ flakes can significantly modify the surface energy compared with the underlying surface owing to its relatively thick three-atomic-layer thickness. In contrast, preferential wetting of PS on monoatomic layer graphene or h-BN surfaces needs to be differentiated from other 2D materials owing to their wetting transparency. Monolayer graphene and h-BN are relatively opaque for short-range polar interactions (e.g., hydrogen bonds), but partially transparent for long-range dispersive interactions (e.g., van der Waals interactions) owing to their extreme thinness (≈0.34 nm) and chemical inertness.[17,23] Because the wetting of PS and PDMS on the SiO$_2$ surface is governed by van der Waals interactions, monolayer graphene or h-BN may significantly influence the wetting behaviors of PS and PDMS on a SiO$_2$ substrate. Notably, graphene could have a specific π–π interaction with the phenyl side group in PS via overlap between π orbitals, whose strength is comparable to that of typical hydrogen bonding.[24] In the case of h-BN, its polar surface with non-uniform charge distribution arising from the electronegativity difference between nitrogen and boron atoms may facilitate partial delocalization of π electrons. Therefore, it can also form π–π stacking interaction with nonpolar aromatic rings, while presenting a specific atomic arrangement in which the center of the aromatic ring with a relatively low charge density is preferentially located immediately above the nitrogen atom (Figure S2, Supporting Information).[25–27] These specific interactions allow the distinctive wetting behaviors of the PS component, even on the monolayer surfaces, despite the comparable calculated interfacial energies between $\gamma_{graphene-PS} - \gamma_{graphene-PDMS}$ and $\gamma_{h-BN-PS} - \gamma_{h-BN-PDMS}$. Taken together, the effective modification of the substrate surface chemistry by 2D flakes could result in the observed wetting contrast between bare SiO$_2$ and 2D-flake-covered surfaces (Figure 2d).

To clarify the influence of the wetting layer contrast on the alignment of BCP nanodomains, the morphological evolution of BCP nanopatterns near the edge of 2D flakes was investigated using self-consistent field theory (SCFT) calculations (Figure 2f and Experimental section in Supporting Information).[29–30] The left-half region of the system is on bare SiO$_2$, and thus we assign a favorable interaction with PDMS. In contrast, the right-half region corresponds to the 2D graphene surface, which has a preference for PS. As shown in Figure 2f, the PDMS layer preferentially wetted both the top and bottom surfaces of bare SiO$_2$. In the middle of the BCP film layer, PDMS nanocylinders are observed; edge parallel cylinders are partially stabilized immediately next to the 2D edge, but the preferential alignment deteriorates upon the neighboring bare SiO$_2$ surface while moving away from the edge. In contrast, the region above the 2D flakes exhibited excellent preferential orientation along the 2D edge. Although the PDMS layer completely wets the top surface, the PS layer touches the bottom surface. Evidently, the boundary between the 2D flake and bare SiO$_2$ offers strong guidance for cylinder alignment. Notably, the result in Figure 2f is obtained from an initial condition with randomly oriented in-plane cylinders. Repeated simulations with different initial conditions confirmed high reproducibility. Furthermore, to identify the role of PS homopolymers in the self-assembly process, we

plotted the homopolymer density obtained using SCFT calculations (Figure S3, Supporting Information). The plot shows that the homopolymers simply fill in the PS domain, and the homopolymer density is 30% or less throughout the thin film. Thus, we do not expect significant contribution of the homopolymers to the self-assembly, rather than acting as PS fillers and fluidizing the annealing process. Overall, the SCFT calculation successfully verified that the experimentally observed nanodomain alignment was induced by the wetting contrast at the 2D-flake edge.

Motivated by our interesting nanoscale directed self-assembly principle enforced by 2D flakes, highly aligned sub-10-nm-wide GNR arrays were demonstrated (**Figure 3**a). BCP lithography has been frequently exploited for GNR fabrication owing to its genuine patternability for sub-10-nm-scale features, which is inevitably required for the bandgap opening of graphene. Unfortunately, previous approaches for GNR fabrication by BCP lithography have generally relied on supplementary pre-patterned structures prepared by conventional photolithography or imprinting to guide the BCP nanopatterns. Owing to the intrinsic limitation of the pattern quality from conventional lithography, the LER and LWR of BCP nanopatterns could deteriorate, which may significantly degrade the desired semiconducting properties of the resultant GNRs. In contrast, our self-alignment principle for BCP self-assembly can be achieved without pre-guiding patterns while minimizing the defectivity and contamination of GNRs without a multistep process. Moreover, BCP pattern guided by 2D edge could ensure very low levels of LWR and LER as 2.13 and 1.43 nm, respectively (Figure 3b and Figure S4–S6, Supporting Information). These values are obviously lower than any previous values obtained from the PS-b-PDMS BCP with similar molecular weights and other nanopatterning strategies, resulting from the atomic-level sharpness of the guiding 2D edge (**Table 2**). However, this pattern requires further improvement to the level of EUV lithography (c.f. LWR and LER of ≈1.0 and 1.71 nm),[31–33] which is widely used in semiconductor lithography. Nevertheless, we can achieve a similar level of critical dimension to that of EUV lithography more efficiently in terms of process cost and complexity. We expect the proposed DSA method to be a good candidate for large-area nanopatterning that is compatible with EUV lithography.

Another significant contribution to high-quality BCP nanopatterning is the use of thermal annealing instead of solvent vapor annealing. Solvent annealing has been the predominant self-assembly process for high-χ BCPs such as PS-b-PDMS to overcome the non-negligible energy barrier for the defect annihilation process. Unfortunately, the solvent additive significantly lowers the χ value during the solvent annealing process, thereby yielding a relatively thick interfacial width between chemically different nanodomains (between PS and PDMS in this work). This may lead to a high LER/LWR ratio in the final assembled nanopatterns. In contrast, thermal annealing minimizes the interfacial width while maintaining intrinsic high segregation strength between nanodomains. Importantly, upon thermal annealing, an intermittent 2D flake may screen any specific interaction between BCP chains and the surface functionalities from the bottom substrate, such as grafting of PDMS chains on hydroxyl-terminated SiO$_2$,[35] to attain rapid

**ADVANCED
SCIENCE NEWS**

www.advancedsciencenews.com

**ADVANCED
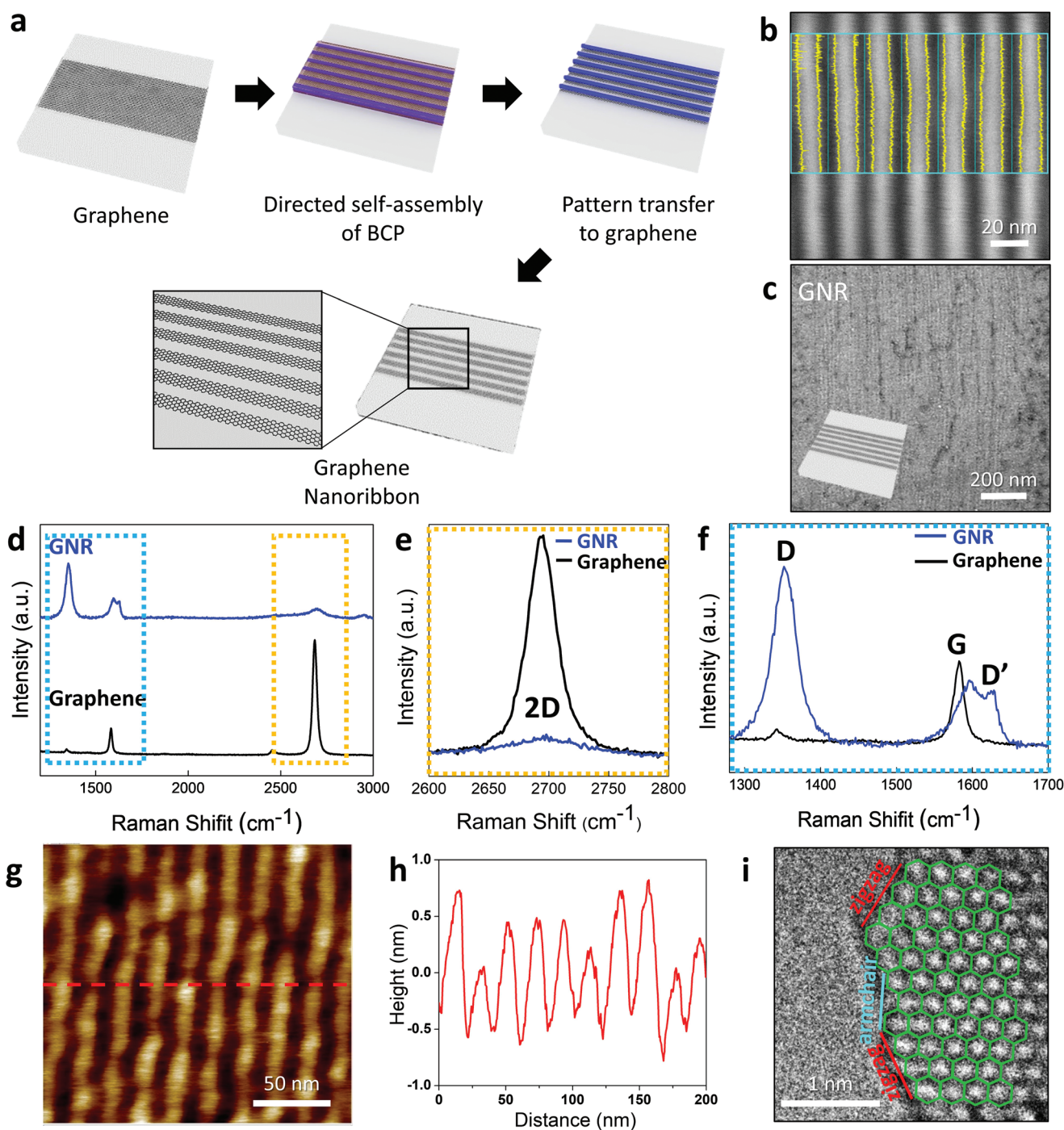MATERIALS**

www.advmat.de

Figure 3. a) Schematic of GNR nanofabrication templating from sub-10-nm-wide 2D edge-directed BCP nanopatterns. b) High-magnification SEM image to analyze patterning parameters. c) Final GNR arrays after removing residual BCP thin film. d) Raman spectra of pristine graphene and GNRs. e) G-band and defect induced D- and D'-band spectra of pristine graphene and GNRs. f) 2D-band spectra of pristine graphene and GNRs. Morphological characterization using g) AFM and h) corresponding height profile. i) GNR edge structure characterized using Cs-TEM.

kinetics for the highly ordered minimal defective structure, even without the lubrication effect from the solvent annealing process.

Subsequent pattern transfer toward the underlying graphene layer was performed using typical reactive ion etching (RIE). After removing the top PDMS layer using brief CF_4 plasma,

a nanoscale stripe pattern was transferred to the bottom graphene layer using O_2 plasma along with the in-plane PDMS nanocylinder array as an etching mask. After successful pattern transfer, the BCP residue remaining on the GNR surfaces could be effectively removed by additional brief O_2 plasma etching and subsequent solvent washing.

Table 2. Comparison of patterning parameters calculated from the line patterns directed by graphene edge and other nanopatterning strategies.

Directing principle	Mean CD [nm]	LWR [nm]	LER [nm]
Edge-directed	10.93	2.13	1.43
Graphoepitaxy	14.58	3.00	1.84
Chemoepitaxy[57]	11	≈2.50	≈2.80
Nanoimprinting[58]	10	2.1	2.40
EUV lithography[32]	≈10	≈1.0	1.71

Figure 3c presents the sub-10 nm GNR arrays produced in this study. We systematically characterized the GNR arrays using spectroscopic and morphological analyses. First, Raman spectroscopy was performed as a general tool to confirm the number of layers of graphene,[35–38] doping state, and defect level.[39] As shown in Figure 3d, several distinctive features were observed between the unpatterned pristine graphene flakes and the GNRs. The intensity ratio between the 2D and G bands (I_{2D}/I_G) for the unpatterned graphene was ≈4, verifying the monolayer characteristics.[40] For a more detailed analysis, the measured Raman spectra were magnified in two parts: the 2D band (Figure 3e) and D-, D′-, and G bands (Figure 3f). As shown in Figure 3e, the 2D peak intensity of the GNR was much lower than that of the unpatterned graphene sheet.

Generally, the 2D band spectrum of graphene originates from resonant Raman scattering with two-phonon emission, which is proportional to the areal density of sp^2 bonded carbon atoms.[41] Thus, the lower level of the GNR 2D band spectrum results from the lower amount of remaining sp^2 carbons after etching. In Figure 3f, the G-band spectra, originating from the doubly degenerate zone center E_{2g} mode,[43–43] are shown with 1D defect-induced D- and D′ bands. For pristine graphene, the G band shows a remarkably high intensity, whereas the two defect-associated peaks exhibit negligible intensities. In contrast, the corresponding spectrum for GNRs exhibits several distinct characteristics: augmentation of the D-band spectra and emergence of the D′ band, which are absent in the unpatterned graphene. This is evidence of edge site formation during the fabrication of GNR, because the D- and D′-bands originate from scattering at the ribbon edges.[42]

Additional analyses, including atomic force microscopy (AFM) and transmission electron microscopy (TEM), were conducted for in-depth morphological characterization of GNR. Figure 3g represents an in-plane AFM image of the aligned GNR array with a periodic interval. The height profile is indicated by the red dashed line (Figure 3h). The average width of the GNR was ≈10 nm, which matched the diameter of the in-plane PDMS cylinders that served as an etching mask for nanoribbon formation. Figure 3i shows moderate edge roughness along with a random mixture of zigzag and armchair edges.

Utilizing an unprecedented simple fabrication process based on the nanoscale directed assembly principle, our GNR arrays could be readily exploited as a channel for field-effect transistors (FETs). A typical back-gated FET structure was employed for this purpose (**Figure 4**a; the inset and detailed fabrication process are demonstrated in the Supporting materials).
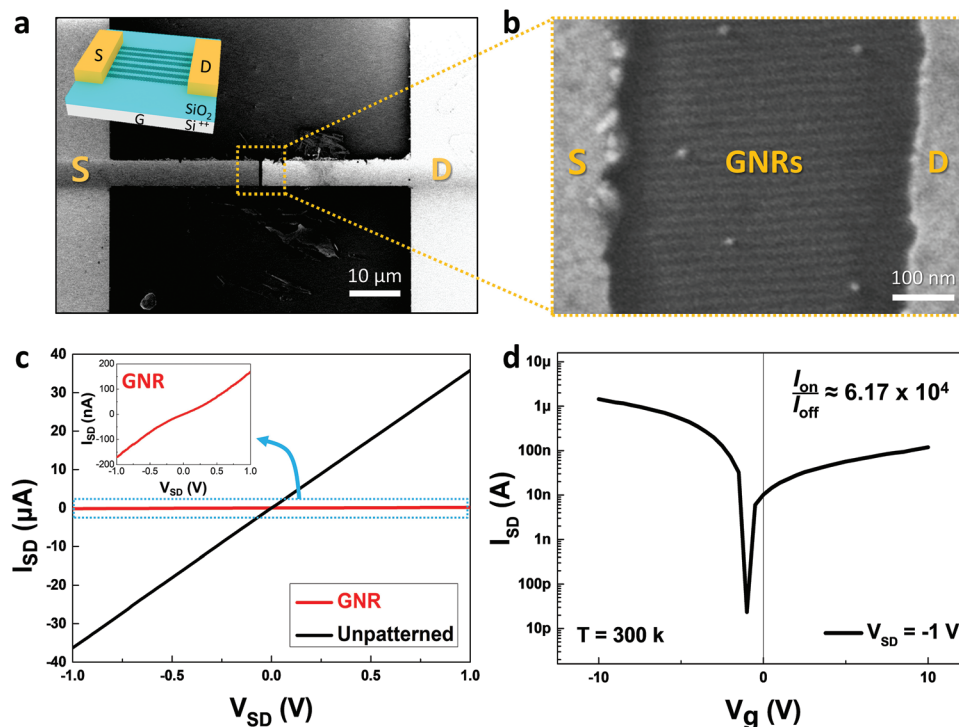

Figure 4. a) SEM image of GNR-channel field effect transistor. b) SEM images of GNR channel arrays formed between Au electrodes. c) Output characteristics for pristine 2D graphene sheet and GNR exhibiting typical non-linear I–V characteristic of GNR FETs. d) Transfer curves for GNR FETs with the highest on–off ratios.

**ADVANCED
SCIENCE NEWS**

www.advancedsciencenews.com

**ADVANCED
MATERIALS**

www.advmat.de

Figure 4a shows the SEM image of the GNR FET consisting of a GNR channel array positioned between the Au source (marked as S) and drain (marked as D) electrodes. The magnified image in Figure 4b confirms that the GNR array was orthogonally aligned against the Au electrodes. The output (current-voltage) characteristics of the FETs based on unpatterned graphene flakes (black curve) and GNR arrays (red curve) were measured at zero gate voltage ($V_g = 0$ V) under ambient conditions (Figure 4c). The unpatterned graphene flake channel leads to typical metallic behavior arising from the semimetallic nature of pristine graphene.[44] Along with the voltage increase between source and drain (V_{SD}) from –1 V to 1 V, current flow between source and drain (I_{SD}) proportionally increases with a characteristic resistance value of 29.3 mΩ (conductance value of 34.12 S). In contrast, the output characteristic of the GNR FET exhibits a substantial current drop with a non-linear I–V relationship in a similar range of V_{SD} (Figure 4c, inset). This non-linear behavior demonstrates the genuine semiconducting nature of our GNR array enforced by the 1D confinement of charge carriers within a sub-10-nm-level nanoribbon width. The semiconducting characteristics were also confirmed by the transfer curve (i.e., the source–drain current I_{SD} as a function of the gate voltage (V_G) measured under ambient conditions) (Figure 4d).

One of the critical parameters for the performance of FETs is the ratio between the channel currents in the open (I_{On}) and closed states (I_{Off}). This I_{On}/I_{Off} ratio should be as large as possible for two easily distinguishable signal states and low current leakage in the closed state. As shown in Figure 4d, our GNR FET attains the highest switching characteristic with an I_{On}/I_{Off} of ≈6 ×10^4, even under ambient conditions, compared to previously reported GNR FETs.[45–49] In particular, this characteristic is comparable to that of conventional silicon-based FETs.[50–52] This remarkable performance reflects the high structural quality and homogeneity of the GNR arrays generated using our strategy. The maximum transconductance value of the GNR FET was 2.294×10^{-7} S. The performance of several FETs ($N = 2$) manufactured using the current method was also characterized (Figure S7, Supporting Information), and the I_{On}/I_{Off} ratio had an average value of 3.12×10^4.

The noticeably high I_{On}/I_{Off} ratio of our GNR FETs can benefit from two principal aspects. First, our self-aligned nanopatterning enabled a minimal number of processing steps for the GNR fabrication. Previously, BCP lithography-based strategies for GNR fabrication generally required supplementary lithography steps for guide pattern formation. The additional multistep processing could incur defects and contaminations in graphene, which could significantly degrade the electrical properties of GNRs, leading to a low on-state current value (I_{On}). In contrast, our self-alignment strategy requires minimal processing steps to avoid contamination and defect formation. Second, an unprecedented high level of alignment is attained in the BCP nanodomains herein, thereby yielding low LER and LWR, as guided by the atomically flat 2D edge. In contrast to the typical guide pattern prepared by conventional lithography with non-negligible pattern roughness (possibly above the nanoscale), the 2D flat edge offers a minimal roughness pattern guide for BCP self-assembly. Accordingly,

the resultant morphology and associated electrical properties of the GNR array can be optimized with a low LER/LWR. The uniform width and smooth edge of the GNR array can achieve an ideally low I_{Off} and high I_{On} for optimal performance. In addition, the high regularity of GNR structures enabled by well-aligned periodic BCP nanopatterns provides a minimal distribution of electrical characteristics among neighboring GNRs.

3. Conclusion

We have presented a straightforward method to direct the self-assembly of BCPs along the edges of monolayer or few-layer exfoliated 2D materials such as, graphene, MoS_2, and h-BN. The fundamental alignment mechanism based on preferential interfacial wetting was successfully investigated by considering interfacial energies, specific intermolecular interactions, and SCFT calculations. The atomically flat geometry of the 2D-material edge offers an unprecedented low level of LER/LWR in BCP nanopatterns, which is compatible with the EUV-based semiconductor lithographic process. This also clarifies the significance of pre-pattern quality for the ultimate quality of DSA pattern, which has long been controversial. The resultant nanocylinder array with a narrow distribution of cylinder diameter and highly uniform periodicity enables a high-quality sub-10-nm-wide GNR array with noticeable field-effect transistor characteristics. This novel approach highlights the synergistic integration of bottom-up nanofabrication with interesting 2D-material characteristics for electronics, optoelectronics, sensors, etc.

Supporting Information

Supporting Information is available from the Wiley Online Library or from the author.

Conflict of Interest

The authors declare no conflict of interest.

Data Availability Statement

The data that support the findings of this study are available from the corresponding author upon reasonable request.

[1] R. Mas-Ballesté, C. Gómez-Navarro, J. Gómez-Herrero, F. Zamora, *Nanoscale* **2011**, *3*, 20.

[2] G. Fiori, F. Bonaccorso, G. Iannaccone, T. Palacios, D. Neumaier, A. Seabaugh, S. K. Banerjee, L. Colombo, *Nat. Nanotechnol.* **2014**, *9*, 768.

[3] B. Radisavljevic, A. Radenovic, J. Brivio, V. Giacometti, A. Kis, *Nat. Nanotechnol.* **2011**, *6*, 147.

[4] T. Yun, H. M. Jin, D.-H. Kim, K. H. Han, G. G. Yang, G. Y. Lee, G. S. Lee, J. Y. Choi, I.-D. Kim, S. O. Kim, *Adv. Funct. Mater.* **2018**, *28*, 1804508.

[5] C. Huang, C. Li, G. Shi, *Energy Environ. Sci.* **2012**, *5*, 8848.

[6] Y. Jiao, A. M. Hafez, D. Cao, A. Mukhopadhyay, Y. Ma, H. Zhu, *Small* **2018**, *14*, 1800640.

[7] A. J. M. Giesbers, U. Zeitler, S. Neubeck, F. Freitag, K. S. Novoselov, J. C. Maan, *Solid State Commun.* **2008**, *147*, 366.

[8] Z. Chen, Y.-M. Lin, M. J. Rooks, P. Avouris, *Phys. E (Amsterdam, Neth.)* **2007**, *40*, 228.

[9] R. Garcia, A. W. Knoll, E. Riedo, *Nat. Nanotechnol.* **2014**, *9*, 577.

[10] J. D. Cushen, I. Otsuka, C. M. Bates, S. Halila, S. Fort, C. Rochas, J. A. Easley, E. L. Rausch, A. Thio, R. Borsali, C. G. Willson, C. J. Ellison, *ACS Nano* **2012**, *6*, 3424.

[11] H. M. Jin, D. Y. Park, S.-J. Jeong, G. Y. Lee, J. Y. Kim, J. H. Mun, S. K. Cha, J. Lim, J. S. Kim, K. H. Kim, K. J. Lee, S. O. Kim, *Adv. Mater.* **2017**, *29*, 1700595.

[12] S. O. Kim, H. H. Solak, M. P. Stoykovich, N. J. Ferrier, J. J. De Pablo, P. F. Nealey, *Nature* **2003**, *424*, 411.

[13] C.-C. Liu, E. Franke, Y. Mignot, R. Xie, C. W. Yeung, J. Zhang, C. Chi, C. Zhang, R. Farrell, K. Lai, H. Tsai, N. Felix, D. Corliss, *Nat. Electron.* **2018**, *1*, 562.

[14] H. M. Jin, S. H. Lee, J. Y. Kim, S.-W. Son, B. H. Kim, H. K. Lee, J. H. Mun, S. K. Cha, J. S. Kim, P. F. Nealey, K. J. Lee, S. O. Kim, *ACS Nano* **2016**, *10*, 3435.

[15] K. G. A. Tavakkoli, K. W. Gotrik, A. F. Hannon, A. Alexander-Katz, C. A. Ross, K. K. Berggren, *Science* **2012**, *336*, 1294.

[16] S.-J. Jeong, J. E. Kim, H.-S. Moon, B. H. Kim, S. M. Kim, J. B. Kim, S. O. Kim, *Nano Lett.* **2009**, *9*, 2300.

[17] J. Rafiee, X. Mi, H. Gullapalli, A. V. Thomas, F. Yavari, Y. Shi, P. M. Ajayan, N. A. Koratkar, *Nat. Mater.* **2012**, *11*, 217.

[18] C. A. Hunter, J. K. M. Sanders, *J. Am. Chem. Soc.* **1990**, *112*, 5525.

[19] R. M. Jacobberger, V. Thapar, G.-P. Wu, T.-H. Chang, V. Saraswat, A. J. Way, K. R. Jinkins, Z. Ma, P. F. Nealey, S.-M. Hur, S. Xiong, M. S. Arnold, *Nat. Commun.* **2020**, *11*, 4151.

[20] Z. Tang, Z. Xu, C. Cai, J. Lin, Y. Yao, C. Yang, X. Tian, *Macromol. Rapid Commun.* **2020**, *41*, 2000349.

[21] C. A. Silvera Batista, R. G. Larson, N. A. Kotov, *Science* **2015**, *350*, 1242477.

[22] V. Harish, D. Tewari, M. Gaur, A. B. Yadav, S. Swaroop, M. Bechelany, A. Barhoum, *Nanomaterials* **2022**, *12*, 457.

[23] X. Liu, Z. Zhang, W. Guo, *Phys. Rev. B* **2018**, *97*.

[24] J. M. Yun, S. Park, Y. H. Hwang, E.-S. Lee, U. Maiti, H. Moon, B.-H. Kim, B.-S. Bae, Y.-H. Kim, S. O. Kim, *ACS Nano* **2014**, *8*, 650.

[25] Y.-T. Liu, X.-M. Xie, X.-Y. Ye, *Chem. Commun.* **2013**, *49*, 388.

[26] X. Chen, S. Jia, N. Ding, J. Shi, Z. Wang, *Environ. Sci.: Nano* **2016**, *3*, 1493.

[27] G. Gou, B. Pan, L. Shi, *ACS Nano* **2010**, *4*, 1313.

[28] Y.-B. Yang, S. J. Park, P. Kim, J. U. Kim, *Soft Matter* **2013**, *9*, 5624.

[29] Y.-B. Yang, Y. J. Choi, S. O. Kim, J. U. Kim, *Soft Matter* **2015**, *11*, 4496.

[30] F. Drolet, G. H. Fredrickson, *Phys. Rev. Lett.* **1999**, *83*, 4317.

[31] R. Bonam, C.-C. Liu, M. Breton, S. Sieg, I. Seshadri, N. Saulnier, J. Shearer, R. Muthinti, R. Patlolla, H. Huang, *Proc. SPIE* **2017**, *10143*, 101431A.

[32] E. Liu, K. Lutker-Lee, Q. Lou, Y.-M. Chen, A. Raley, P. Biolsi, *Proc. SPIE* **2021**, *11615*, 1161506.

[33] T. Wada, C.-Y. Hsieh, A. Ko, P. Biolsi, *Proc. SPIE* **2019**, *10963*, 109630I.

[34] V. M. Litvinov, H. Barthel, J. Weis, *Macromolecules* **2002**, *35*, 4356.

[35] A. C. Ferrari, J. C. Meyer, V. Scardaci, C. Casiraghi, M. Lazzeri, F. Mauri, S. Piscanec, D. Jiang, K. S. Novoselov, S. Roth, A. K. Geim, *Phys. Rev. Lett.* **2006**, *97*, 187401.

[36] A. Gupta, G. Chen, P. Joshi, S. Tadigadapa, Eklund, *Nano Lett.* **2006**, *6*, 2667.

[37] D. Graf, F. Molitor, K. Ensslin, C. Stampfer, A. Jungen, C. Hierold, L. Wirtz, *Nano Lett.* **2007**, *7*, 238.

[38] A. C. Ferrari, D. M. Basko, *Nat. Nanotechnol.* **2013**, *8*, 235.

[39] L. G. Cançado, A. Jorio, E. H. M. Ferreira, F. Stavale, C. A. Achete, R. B. Capaz, M. V. O. Moutinho, A. Lombardo, T. S. Kulmala, A. C. Ferrari, *Nano Lett.* **2011**, *11*, 3190.

[40] D. Yoon, H. Moon, Y.-W. Son, J. S. Choi, B. H. Park, Y. H. Cha, Y. D. Kim, H. Cheong, *Phys. Rev. B* **2009**, *80*, 125422.

[41] D. Bischoff, J. Güttinger, S. Dröscher, T. Ihn, K. Ensslin, C. Stampfer, *J. Appl. Phys.* **2011**, *109*, 073710.

[42] M. Huang, H. Yan, C. Chen, D. Song, T. F. Heinz, J. Hone, *Proc. Natl. Acad. Sci. USA* **2009**, *106*, 7304.

[43] T. M. G. Mohiuddin, A. Lombardo, R. R. Nair, A. Bonetti, G. Savini, R. Jalil, N. Bonini, D. M. Basko, C. Galiotis, N. Marzari, K. S. Novoselov, A. K. Geim, A. C. Ferrari, *Phys. Rev. B* **2009**, *79*, 205433.

[44] S. D. Sarma, S. Adam, E. H. Hwang, E. Rossi, *Rev. Mod. Phys.* **2011**, *83*, 407.

[45] X. Li, X. Wang, L. Zhang, S. Lee, H. Dai, *Science* **2008**, *319*, 1229.

[46] X. Wang, Y. Ouyang, X. Li, H. Wang, J. Guo, H. Dai, *Phys. Rev. Lett.* **2008**, *100*, 206803.

[47] X. Liang, S. Wi, *ACS Nano* **2012**, *6*, 9700.

[48] J. G. Son, M. Son, K.-J. Moon, B. H. Lee, J.-M. Myoung, M. S. Strano, M.-H. Ham, C. A. Ross, *Adv. Mater.* **2013**, *25*, 4723.

[49] S.-J. Jeong, S. Jo, J. Lee, K. Yang, H. Lee, C.-S. Lee, H. Park, S. Park, *Nano Lett.* **2016**, *16*, 5378.

[50] S. D. Suk, K. H. Yeo, K. H. Cho, M. Li, Y. Y. Yeoh, S. Lee, S. M. Kim, E. J. Yoon, M. S. Kim, C. W. Oh, S. H. Kim, D. Kim, D. Park, *IEEE Trans. Nanotechnol.* **2008**, *7*, 181.

[51] T. Tahara, H. Koike, M. Kameno, T. Sasaki, Y. Ando, K. Tanaka, S. Miwa, M. Suzuki, M. Shiraishi, *Appl. Phys. Express* **2015**, *8*, 113004.

[52] Y. Hashim, in *2017 IEEE Regional Symp. on Micro and Nanoelectronics (RSM)*, IEEE, Piscataway, NJ, USA **2017**, pp. 231–234.

[53] D. K. Owens, R. C. Wendt, *J. Appl. Polym. Sci.* **1969**, *13*, 1741.

[54] M. Annamalai, K. Gopinadhan, S. A. Han, S. Saha, H. J. Park, E. B. Cho, B. Kumar, A. Patra, S.-W. Kim, T. Venkatesan, *Nanoscale* **2016**, *8*, 5764.

[55] N. Rathod, S. G. Hatzikiriakos, *Polym. Eng. Sci.* **2004**, *44*, 1543.

[56] S. Wu, *J. Polym. Sci., Part C: Polym. Symp.* **1971**, *34*, 19.

[57] L. Wan, R. Ruiz, H. Gao, K. C. Patel, T. R. Albrecht, J. Yin, J. Kim, Y. Cao, G. Lin, *ACS Nano* **2015**, *9*, 7506.

[58] S.-M. Park, X. Liang, B. D. Harteneck, T. E. Pick, N. Hiroshiba, Y. Wu, B. A. Helms, D. L. Olynick, *ACS Nano* **2011**, *5*, 8523.